Controlling the static and ultra-fast infrared optical response of Al:ZnO through nanostructuration

Tersilla Virgili†, Luca Bursi†, Riccardo Magrin Maffei, Michele Guizzardi, Andrea Villa, Alessandro di Bona, Andrea Mescola, Gian Carlo Gazzadi, Arrigo Calzolari, Stefania Benedetti**

†T.V. and L.B. contributed equally to the work

Tersilla Virgili, Michele Guizzardi,
Istituto di Fotonica e Nanotecnologie, CNR, P.zza Leonardo Da Vinci 32, 20132 Milano, Italy
E-mail: tersilla.virgili@cnr.it

Andrea Villa
Dipartimento di Fisica, Politecnico di Milano, P.zza Leonardo da Vinci 32, 20132 Milano, Italy

Luca Bursi, Riccardo Magrin Maffei
Dipartimento di Scienze Fisiche, Informatiche e Matematiche, Università di Modena e Reggio Emilia, via Campi 213/a, 41125, Modena, Italy;
CNR Istituto Nanoscienze, via Campi 213/a, 41125, Modena, Italy
E-mail: luca.bursi@unimore.it

Alessandro di Bona, Andrea Mescola, Gian Carlo Gazzadi, Arrigo Calzolari, Stefania Benedetti
CNR Istituto Nanoscienze, via Campi 213/a, 41125, Modena, Italy
E-mail: stefania.benedetti@nano.cnr.it

Keywords: transparent conducting oxide, focused ion beam, nanostructuration, transient absorption spectroscopy

Abstract

Aluminum-doped zinc oxide (AZO) is one of the most promising n-type transparent conductive oxides, valued for its low cost, high visible transparency, and low electrical resistivity. Its plasmonic response in the near-infrared region tunable via dopant concentration and the low optical losses make it a promising material for complementary metal oxide semiconductor CMOS-compatible photonic applications. Here, we investigate the role of nanostructuration in the optical properties of engineered AZO metasurfaces. We design, fabricate, and compare periodic arrays of nanocylinders, nanorods, and L-shaped nanostructures (nano-Ls) as a function of their relevant structural parameters. Selected metasurfaces are fabricated after an electron beam lithography and focused ion beam process. They are characterized from both a static and a dynamic point of view via ultra-fast MID-IR pump probe technique, demonstrating marked differences of the optical behavior in the nanostructures. Our results establish that it is possible to modify and control the ultra-fast response of AZO metasurfaces through nanostructuration making them promising building blocks for infrared plasmonics and nanophotonic applications where metal-free and CMOS-compatible platforms are advantageous.

1. Introduction

Transparent conducting oxides (TCOs) uniquely combine high optical transparency and electrical conductivity, showing an epsilon-near-zero (ENZ) behavior in the near- to mid-infrared (NIR – MIR) spectral range, with low losses and ultrafast switching capabilities.[1,2,3] Their optical response can be intrinsically tuned within the telecommunication window by deposition conditions,[4,5] post-growth treatments,[6,7] or active tuning by means of electrical or optical stimuli.[8,9,10,11] An additional degree of control over the system's response is achieved through nanostructuration, particularly via the realization of metasurfaces. Photonic metasurfaces are artificially fabricated nanostructures (NS) with subwavelength features that confine, guide and control the propagation of light at the nanoscale, enabling unique optical properties and functionalities that are not accessible with conventional materials. These

metasurfaces open the way to many possible applications in photonics,[12] spanning from beam steering, focusing, and optical switching, to holography using ultrathin optical components.[13] Optical metasurfaces are most commonly made of noble metals (especially Au, Ag and Cu). However, their high charge density makes them unsuited for applications in the NIR-MIR range. In contrast, TCOs, because of their lower and controllable injected charge, are the materials of choice for these applications. Nevertheless, the requirement for maintaining electrical homogeneity across the sample makes the nanofabrication of doped metal-oxides a technological challenge.

A few studies have been reported on nanofabrication of TCOs, and AZO in particular, by means of electron beam lithography (EBL), focused ion beam (FIB),[14,15] or guided by catalyst.[16] Most reported TCO nanostructures typically have lateral sizes exceeding 500 nm. Achieving sub-100 nm nanostructures with precise shape control requires addressing several critical factors. First, a uniform, dense, and compact film is essential. Granular films with large grains and irregular shapes complicate the patterning and the control of nanostructures, often leading to poorer resolution in lithographic techniques.[17] Second, when using electron beam lithography (EBL) with a lift-off process, films deposited by sputtering present resolution challenges due to deposition on the sidewalls of the resist. EBL typically requires thin resists to reduce lateral nanostructure size, which then limits their aspect ratio. Similarly, sputter deposition conditions need to be carefully controlled to minimize sidewall deposition, and high-energy electron beams or chemical etching are sometimes necessary. In contrast, Focused Ion Beam (FIB) directly fabricates nanostructures, significantly mitigating many of these fabrication limitations. While FIB fabrication can lead to localized material damage, such as a reduction in carrier concentration in materials like ITO metasurfaces, this damage can be easily restored through annealing treatments.[18]

Combining TCOs tunability with FIB nanostructuration enables further control over local electromagnetic fields and carrier dynamics, opening the way to engineering new types of photonic components, and designing new photophysics properties of radiation by using subwavelength resonant nanostructures.[19,20] The promising advances in hot carrier physics and technology rely on the understanding of the nonequilibrium mechanisms that regulate the interaction between light, the electrons in the material and the environment of the NS.[21,22] Towards this direction, a considerable contribution has come from transient absorption (TA) spectroscopy, rapidly advancing the field of ultrafast optics.[23,24] Femtosecond pump-probe experiments have become a powerful tool to unveil the energy exchange processes governing hot carrier equilibration, by allowing to track their evolution in time.[25] Directly detecting the

excitation and relaxation of collective electron oscillations provides insights into transient microscopic quantities — such as carrier distributions, electronic temperatures, scattering rates, and coherent lifetimes — that are key to explore the fundamental physics of ultrafast response in TCOs, and thus to develop novel optical applications.[26]

In this regard, it has been demonstrated that the optical properties of AZO films can be dynamically addressed on a sub-picosecond timescale by a clever combination of nonlinear inter- and intra-band effects, driven by different wavelength pump pulses.[27] Hence, the modulation of the dynamic refractive index in the ENZ region due to pulsed light, imparts significant nonlinear responses.[28] In particular, following the resonant photoexcitation process, the localized surface plasmon resonances (LSPRs) and the surface plasmons (SPs) quickly dephase, giving rise to a distribution of energetic 'hot' electrons. These out-of-equilibrium carriers undergo ultrafast internal relaxation processes, nowadays pivotal in a variety of applications, from photodetection and sensing to driving photochemical reactions and ultrafast all-optical modulation of light.[25]

In this work, we show the design, nanofabrication, and characterization of AZO metasurfaces below the 100-nm limit produced by means of FIB to understand the role of nanostructuration in the dynamics of the out-of-equilibrium carriers in order to control the modulation of the photophysics and ultrafast dynamics of the plasmonic response of AZO metasurfaces.

2. Results

To investigate the impact of nanostructuration on the optical response of AZO, we theoretically designed three types of metasurfaces: periodic arrays of **i.** nanocylinders, **ii.** nanorods, and **iii.** L-shaped NSs (nano-Ls), as illustrated in Figure 1. The geometrical models were constructed by using state-of-the-art continuum electromagnetic descriptions, as detailed in the "Numerical simulations" section. To ensure consistency between theory and experiments, we simulated the optical properties of the NSs, by using the experimental permittivity spectra measured for an AZO thin film (Al 4 at.%),[5] grown under the same conditions as the ones used for the metasurfaces nanofabrication. We systematically explored the influence of geometry—namely size, shape, and lattice periodicity—on the optical response of the metasurfaces. The relevant structural parameters for each geometry are defined in Figure 1(a,d,g). Their effect on the spectral position and intensity of the main absorption resonance is summarized in Figure 1(b,e,h) and in Figures S1–S7 of the Supporting Information (SI).

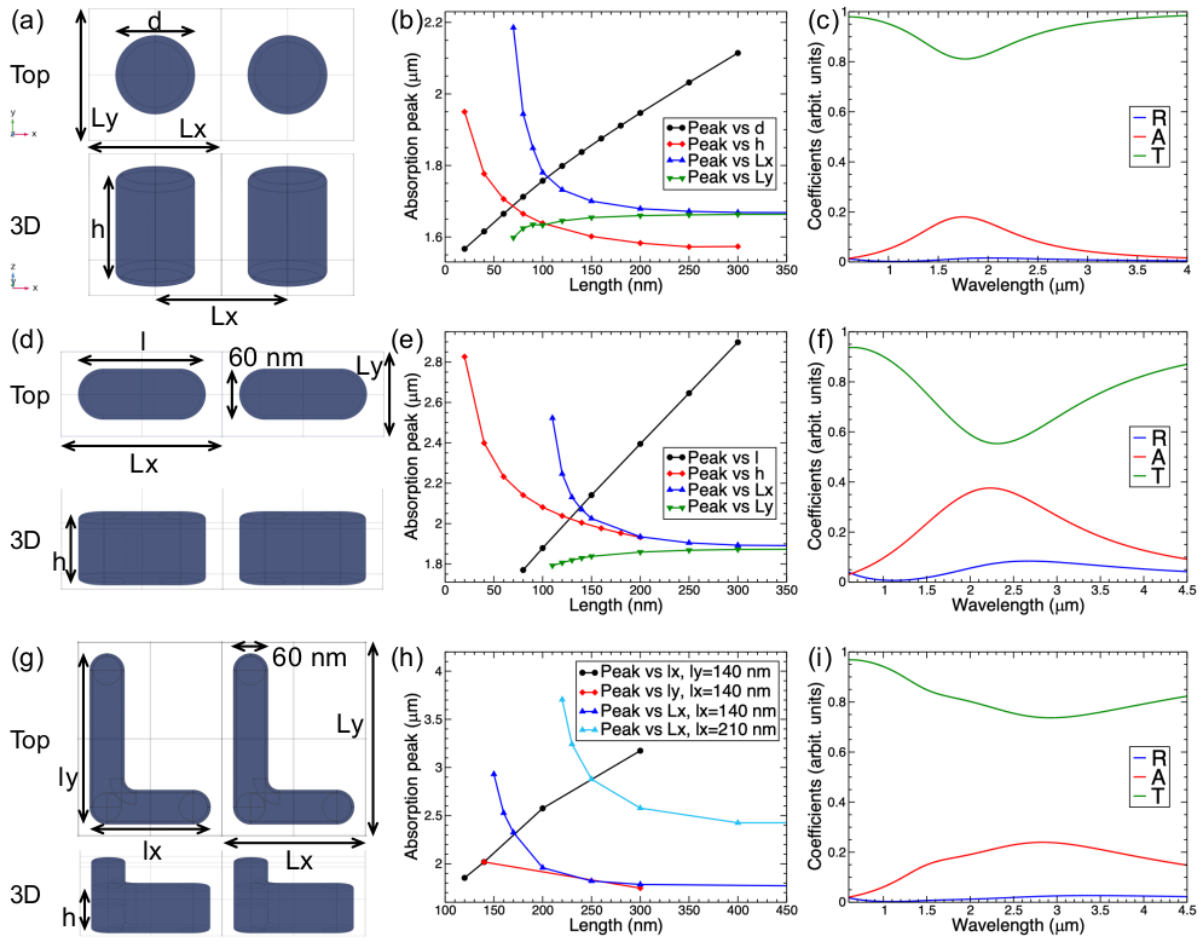

Figure 1: *(a,d,g) Schematics of the geometrical models used in the simulations of AZO metasurfaces (top and side, perspective views), illustrating the definition of relevant structural parameters. (b,c,e,f,h,i) Simulated optical responses for periodic arrays of (a–c) nanocylinders, (d–f) nanorods, and (g–i) nano-Ls. (b,e,h) Resonance wavelengths extracted from absorption spectra simulated as a function of selected geometrical parameters. (c,f,i) Normalized reflection (R), absorption (A), and transmission (T) spectra as a function of wavelength, simulated for the structures with optimized geometries. In (a), d and h denote the nanocylinder diameter and height, respectively. In (d), l and h correspond to the length (along the x-axis) and height of the nanorods, respectively. In (g), lx, ly, and h are the lengths of the arms of the nano-Ls along the x- and y-axes, and their height, respectively. In panels (a,d,g), Lx and Ly represent the lateral dimensions of the simulation cell (periodically replicated in-plane via periodic boundary conditions), corresponding to the center-to-center distance between neighboring nanostructures in the array, along the x and y directions, respectively.*

Our analysis reveals that increasing the size of the nanostructures along the x-axis (i.e., the polarization direction of the incident light) causes a pronounced redshift and enhancement of the absorption peak. Conversely, increasing the height (along the z-axis) or the lateral size (along the y-axis)—perpendicular to the polarization direction, leads to a blueshift and a moderate increase of the absorption intensity. However, the blueshift saturates for heights and widths above ~200 nm and has a weaker impact than elongation along the x-axis. The role of inter-particle coupling was investigated by varying the center-to-center spacing along the x and y directions, i.e., L_x and L_y (Figure 1). Increasing L_x results in a blueshift and reduced intensity of the absorption peak, while increasing L_y leads to a redshift and slight intensity enhancement.

For $L_{x,y} \gtrsim l_{x,y} + 150$ nm, where $l_{x,y}$ indicates the length of the NS along the x and y axis, respectively, the resonance energies and intensities asymptotically converge to those of isolated NSs, indicating negligible inter-NS coupling.

The calculated absorption of these AZO metasurfaces is inherently weaker than that expected for comparable plasmonic metal NSs, which exhibit stronger and narrower resonances in the visible/ultraviolet spectral range. This also explains the negligible enhancement from lattice plasmon resonances in such systems. Since the LSPR energy of the NSs lies in the infrared, achieving significant coupling between LSPR and lattice modes would require lattice periods on the order of 1 μm, which is impractical given the intrinsic weaker response of the individual nanostructures. As such, lattice effects remain marginal in simulations and are not expected to yield experimentally detectable signatures in AZO metasurfaces of this type.

Based on these results and fabrication constraints—particularly the minimum achievable feature sizes and the experimental spectral window between 1 and 2 μm—we optimized the geometries to maximize the absorption in this range. The final selected designs feature a ~40 nm border-to-border pitch and the following parameters: **i.** nanocylinders: diameter $d = 60$ nm, height $h = 80$ nm, $L_X = L_y = 100$ nm; **ii.** nanorods: length $l = 150$, height $h = 80$ nm, $L_x = 190$ nm, $L_y = 100$ nm; **iii.** nano-Ls: arm lengths $l_x = 200$ nm and $l_y = 300$ nm, height $h = 80$ nm, $L_x = 250$ nm, $L_y = 350$ nm.

Figure 1(c,f,i) reports the normalized reflection (R), absorption (A), and transmission (T) coefficients for the optimized structures. Nanorod metasurface exhibits the highest absorption, twice as intense as that composed of nanocylinders, and nearly double of the nano-Ls one. This suggests that nanocylinders are not a good choice for the realization of AZO metasurfaces. Notably, the absorption spectrum of the nano-Ls array shows two distinct features: a peak near 1.5 μm and a broader, more intense resonance centered around 2.8 μm. This dual response stems from the anisotropic geometry of the nano-Ls and offers the opportunity to investigate directionally dependent optical modes. The inclusion of a transparent substrate (e.g., MgO) in the simulations does not change this scenario, giving only a uniform reduction of the peak intensity and slight redshift with respect to air, as shown in Figures S8–S10 of the SI.

Following the theoretical predictions, we fabricated by FIB two AZO metasurfaces on MgO(001) substrate: one composed of nanorods and one composed of nano-Ls, both having the optimal geometrical parameters derived from numerical simulations. AZO films were grown at room temperature on MgO(001) double-side polished substrates by co-depositing with

magnetron sputtering from ZnO and Al targets. Al doping was set to the optimal doping concentration of ~4 at. %,[5] checked by Energy Dispersive X-ray Spectroscopy (EDX). Film thickness was 100 nm and it was controlled during deposition by a calibrated quartz microbalance and subsequently by means of a stylus profilometer. Prior to the fabrication of the NSs, the quality of the substrate film was assessed in terms of grain morphology and surface compactness. SEM and AFM analyses revealed a densely packed granular structure with an

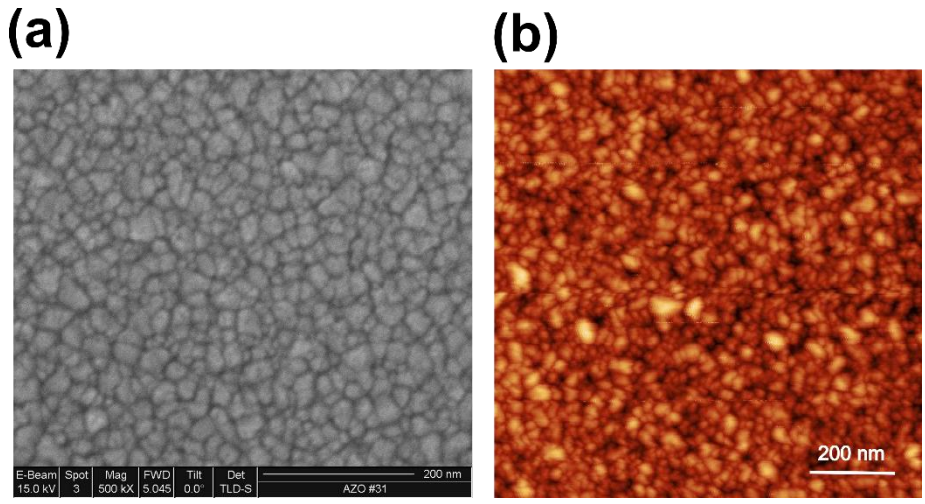

Figure 2: (a) SEM and (b) AFM image of 100 nm AZO 4 at.% film.

average grain diameter of approximately 20 nm and an RMS surface roughness of 2.35 nm (Figure 2). These values confirm the film's suitability as a uniform and stable base for the subsequent nanostructure fabrication.

The choice of transparent MgO substrate poses a limitation during FIB nanofabrication. We need to avoid spurious signals from the surrounding continuous film during pump probe spectroscopy. At the same time, due to the strong insulating character of MgO, the charge accumulation in the area during fabrication must be limited to the minimum when NSs are completely separated from the continuous film. To overcome this limit, we realized by EBL an area without AZO surrounding the NSs array and connected it through bridges to the continuous film during the fabrication process, to maintain electrical continuity and avoid charging during ion irradiation (Figure S11, see Experimental section for details). Once the pattern was finished the bridges have been disconnected. A sketch and SEM images of the obtained AZO metasurfaces are shown in Figure 3a for nanorods and in Figure 3b for nano-Ls. The resulting sizes are derived from SEM images and reported in the sketches: the nano-rods have $l = 150$ nm and are 55 nm wide, with a center-to-center pitch $L_x = 220$ and $L_y = 110$ nm; the nano-Ls have $l_x = 200$ nm and $l_y = 315$ nm, with a 50 nm border-to-border pitch in both directions (corresponding to $L_x = 250\,nm$ and $L_y = 365\,nm$) in good accordance with the values

obtained from the simulations. The ion dose, determined by the ion beam current and the number of repetitions of the beam scanning the chosen area, was calibrated in order to remove completely the AZO film between the NSs. The arrays are fabricated by repetition of a smaller area; hence they appear as collections of "tiles" of nanostructures separated by grooves due to the overlapping of the ion beam scan.

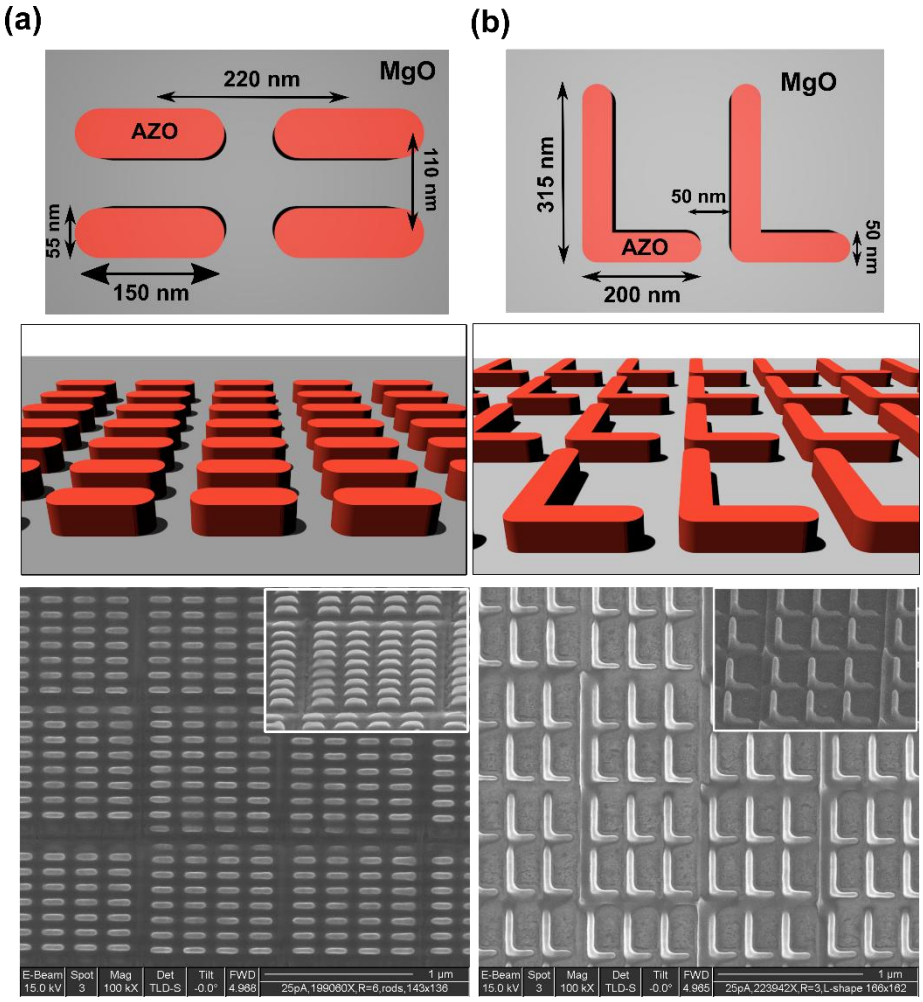

Figure 3: Sketches and SEM images of the arrays of (a) nanorods and (b) nano-Ls obtained by FIB on MgO(001). SEM images are measured at 0° tilt view, while insets are taken with 52° tilt view.

To understand how nanostructuration changes the optical response in time we performed ultrafast spectroscopy measurements with fs time resolution on our metasurface samples. Measurements on the continuous films are also performed for comparison. All measurements are discussed in terms of the fractional change in the transmitted probe signal:

$$\Delta T/T(t)=(T_{ON}(t)-T_{OFF})/T_{OFF}\,, \quad (1)$$

where $T_{ON}(t)$ and T_{OFF} are the transmitted (T) probe signal with and without the optical pump, respectively, and t is the pump-probe delay. Further details can be found in the "Pump-probe spectroscopy" Experimental section.

In AZO film at 4 at.% dopant concentration and 100 nm thickness the absorption spectrum is characterized by a band gap of 330 nm (3.8 eV) and a cross-over frequency at around 1700 nm (ω_p=0.73 eV) due to free carrier absorption, in agreement with previous reports.[29] We then expect the surface plasmon resonance (SPR) to be red-shifted at around 2400 nm (0.52 eV), due to the interface with air. Figure 4 shows the pump probe spectra on the AZO thin film. Although SPR excitation is theoretically not possible in AZO thin films due to the momentum mismatch between light and plasmons,[30] the presence of sub-wavelength surface defects — such as surface roughness (see Figure 2) — can enable SPR photoexcitation even in the absence of phase-matching techniques (e.g., prisms or gratings).[31,32] This effect has been observed for several plasmonic systems, such as Ag thin films.[33,34]

In our experiment, the pump has been tuned at ~1600 nm within the plasmon resonance band, while the probe covers from 325 nm to 500 nm (Figure 4a) and from 1200 nm to 2000 nm (Figure 4b). At time zero the transient differential transmission signal presents a negative band assigned to photoinduced absorption (PIA) peaked at 340 nm that decays to zero in around 1 ps. The NIR region is dominated by a positive band extending until 2000 nm, that after ~100 fs becomes negative and then decays to zero.

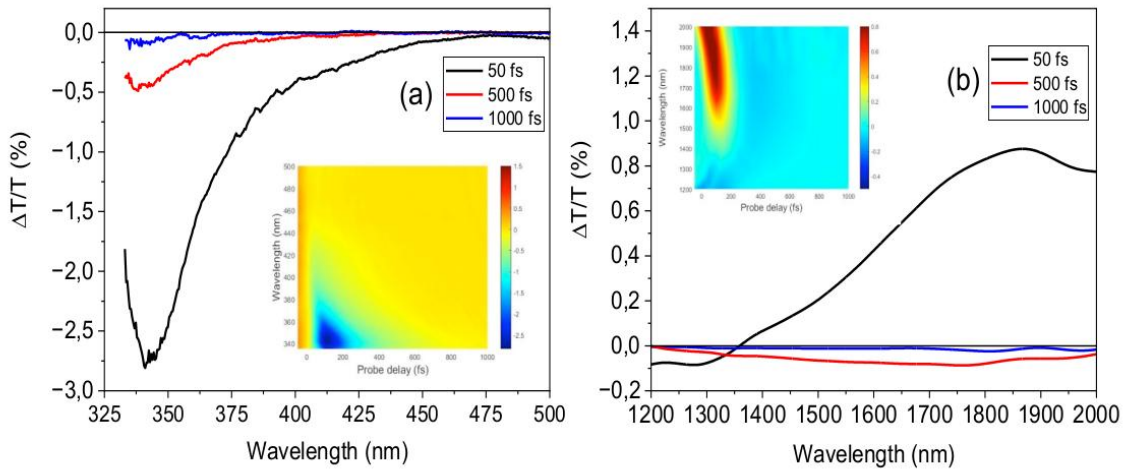

***Figure 4**: (a) Transient differential transmission spectra at different probe delays for the AZO film after 1600nm pump excitation in (a) the UV-visible and (b) NIR spectral region. In the inset, transient differential transmission maps as a function of delay time t and probe photon energy are shown.*

Figure 5 shows the two-dimensional transient differential transmission maps and the decay dynamics at 1800 nm (inset) for the nanorods and nano-Ls after pump excitation at 3000 nm. In this case, the pump energy has been chosen on the basis of the NSs simulations to match the plasmon resonance of both arrays, while the probe region has been restricted between 1200 nm to 2000 nm. After the excitation a positive ΔT/T band is present in both nanostructure arrays, as for the AZO film. However, at longer delay times, the nano-Ls behave like the film and the signal becomes negative, while in the nanorods the signal goes to zero and no negative contribution is present. This is a clear indication that nanofabrication has a role in the ultra-fast photo-physics of AZO metasurfaces.

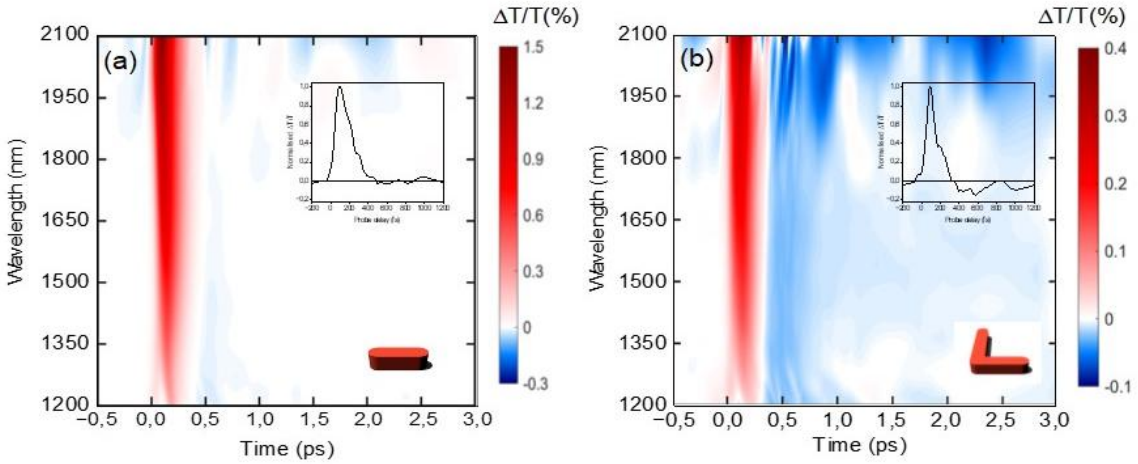

***Figure 5**: Transient differential transmission maps as a function of delay time t and probe photon energy measured for (a) the nanorods and (b) the nano-Ls metasurfaces. In the inset, the time decay at 1800 nm for the two structures.*

3. Discussion

Upon pump excitation, the plasma of the hot electrons undergoes a dephasing on a sub-100 fs time scale. After this time, the energy imparted by the pump is thermalized among the free electrons within the conduction band, increasing their temperature. For the Fermi−Dirac statistics, this increase in the electronic temperature shifts the state occupancy within the conduction band toward high-energy states, while reducing the population of low-energy states. This electronic heating has the net effect of shifting the absorption onset between the valence and the conduction band to lower energy. This is because the states near the conduction band

minimum (CBM) that were occupied at room temperature are now depopulated as a result of SPR excitation.[35] The presence of a hot-electron population induced by an electronic temperature higher than the room temperature results in an increase of the electron effective mass and in a red-shift or broadening of the plasmon resonance, while the Fermi distribution cools down.[27,36]

The pump-probe spectra in Figure 4a indicate the appearance of a strong PIA band at 340 nm (~3.65eV) near AZO band gap (~3.8eV). As discussed above, the pump excitation produces a net red-shift of the absorption onset between the valence and the conduction band. As a consequence, we assign the negative photoinduced absorption band to interband transitions that become available after the electronic heating induced by the SPR excitation. The spectra in the NIR region (Figure 4b) show an instantaneous red shift (increase of transmission, positive $\Delta T/T$) with a subsequent broadening (decrease of transmission, negative $\Delta T/T$) of the plasmonic resonance absorption. Following the interpretation proposed by A. Schirato et al,[25] the analysis of this plasmonic response requires two different electron populations after pump excitations. Within the first hundred femtoseconds, hot carriers undergo internal, non-radiative relaxation processes, evolving from a non-thermal to a thermalized energy distribution via electron–electron (e-e) scattering. This picture accounts for the dynamic contributions of both non-thermal and subsequently thermalized carrier populations.

To prove this statement, we analyzed the temporal decay of the transient signals in AZO film at 340 nm and at 1700 nm by performing a numerical fit of the $\Delta T/T$ dynamics (see SI for more details). Figure 6 shows the comparison between the experimental dynamics (open squares) at 340 nm (black) and at 1700 nm (red) and the theoretical fits (solid lines). The fits indicate the presence of two electron populations: one generated instantaneously, called non-thermal population, characterized by a decay time $\tau_{nt} \sim 100$ fs; and a second thermalized population generated by the relaxation of the first, with a decay time $\tau_t \sim 300$ fs. The two dynamics are fitted considering that these populations, at 1700 nm, produce an instantaneous red shift of the plasmonic resonance (positive $\Delta T/T$ transient signal) and then a consequent broadening (negative transient signal). At 340 nm, both carrier populations contribute to the observed negative $\Delta T/T$ decay (see Figure S14 and SI for more details).

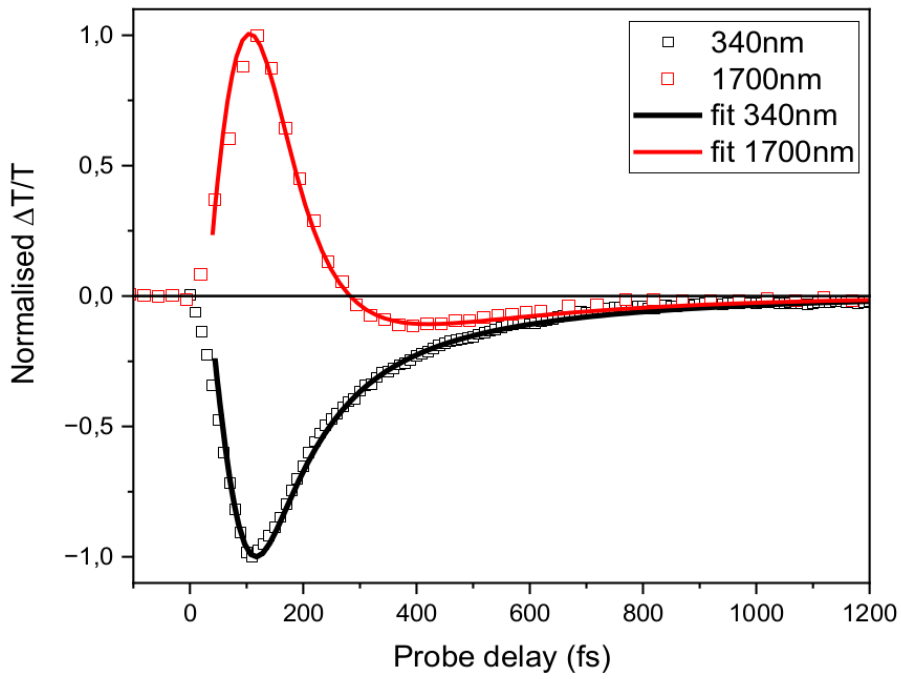

***Figure 6**: Experimental decays (symbols) and theoretical fit (solid line) for the AZO film at 340 nm (black) and at 1700 nm (red).*

While this picture still holds in the case of the nano-Ls metasurface, it cannot be applied to understand the decay for the nanorods array. In the latter case, the smaller sizes (i.e., higher quantum confinement) of the nanorods and of the nanocylinders (see Figure S12-S13) impart a reduction of the density of the available electronic states, not sufficient to sustain and propagate the excitations inside the nanostructures. This implies to neglect the retardation effects across the nanostructures and to have only one electron population responsible for the red-shift of the plasmon resonance.[37] Consequently, the modulation of the ultrafast response in the NSs is essentially governed by their distinct static response — namely, the characteristics of their LSPRs — and is therefore, in principle, controllable through structural design.

4. Conclusions

In this work, we investigated the role of nanostructuration in the optical and plasmonic properties of AZO metasurfaces. Guided by a theoretical design screening, we fabricated two optimized metasurface configurations made of ordered arrays of nanorods and nano-Ls that we compared to the parent AZO thin film. We optically characterized the samples dynamically with an ultra-fast MID-IR pump probe technique, demonstrating marked differences in the optical response of the nanostructures. Our results indicate that the confinement induced by the small nanorod structure allows a very fast decay (100 fs) of the out of equilibrium hot carriers,

while in a larger structure, such as nano-Ls or a corrugated film, the carriers relaxed in a thermalized population that just after 300 fs decays to the ground state. These evidences unambiguously indicate that it is possible to modify and control the plasmonic response of AZO metasurfaces through nanofabrication, both statically and dynamically, making them promising building blocks for infrared plasmonics and nanophotonic applications, where metal-free and CMOS-compatible platforms are advantageous.

5. Experimental Section/Methods

Numerical simulations.

Electromagnetic simulations were carried out by using the commercial software COMSOL Multiphysics, which implements advanced approaches for the solution of partial differential equations based on the finite element method. The optical response of the nanostructures was computed by solving Maxwell's equations in the frequency-domain. Simulations were performed on a single unit cell of the periodic array, with periodic (Floquet) boundary conditions applied along the lateral directions (x and y) to mimic an infinite two-dimensional lattice. To avoid spurious reflections at the boundaries, 50 nm thick perfectly matched layers were implemented along the out-of-plane (z) direction, at the top and bottom boundaries. For all simulated systems, L_x and L_y represent the lateral dimensions of the simulation cell and correspond to the center-to-center distances between adjacent nanostructures in the array, along x and y, respectively. The structural parameters of the different geometries are illustrated in Figure 1. All corners were rounded with spherical caps of 5 nm radius to remove sharp edges. The nanostructures were positioned on top of a 200 nm thick substrate layer and surrounded by a homogeneous background medium. Unless otherwise stated, both the background and substrate media were modeled as air (refractive index $n = 1$). In Figures S9–S11 of the Supporting Information, we show a comparison between the absorption spectra obtained under this assumption and those obtained by modeling the substrate with the measured complex permittivity of the MgO substrate used during system's fabrication.[5]

The system was excited by a normally incident plane wave, linearly polarized along the *x* axis, defined through an input port placed above the structure. A second port, positioned below the structure, collected the transmitted field components. The reflection (R) and transmission (T) coefficients were extracted from the complex S-parameters evaluated at the two ports. The absorption (A) was independently calculated by integrating the time-averaged electromagnetic

power dissipation density (COMSOL variable emw.Qh) over the volume of the nanostructures, capturing all volumetric absorption independently of the direction of scattered fields. The good agreement between the absorption spectra computed in this way and that obtained from the relation $A = 1 - R - T$ confirms the internal consistency of the simulations and validates energy conservation across the entire simulated spectral range for all considered geometries. R, T, and A spectra were obtained by performing the electromagnetic simulations explicitly for a discrete set of wavelengths, in the spectral region of interest, and then interpolating by means of cubic spline functions, as routinely done in frequency-domain finite element approaches. Charge density plots were extracted at selected resonance frequencies to visualize field localization and charge distribution.

Growth and nanostructuration.

AZO films were deposited at room temperature on MgO(001) double-side polished substrates by magnetron sputtering co-deposition from ZnO and Al targets (3" target, purity 99.99%, RF and DC, respectively) in a 5 mTorr Ar working pressure and 3×10^{-6} mbar base pressure. Al doping was set to the optimal doping concentration of ~4 at. %,[5] checked by Energy Dispersive X-ray Spectroscopy (EDX), performed at film surface with a FEI Quanta-200 ESEM. Film thickness was 100 nm and it was controlled during deposition by a calibrated quartz microbalance and subsequently by means of a stylus profilometer.

AZO nanostructures were fabricated by means of Focused Ion Beam. Before FIB fabrication, squared areas of (130x130) μm^2 were prepared by EBL on AZO (Figure S11), separated from the continuous film by some empty areas where AZO is removed by Reactive Ion Etching (RIE) in an Ar plasma (250 W RF power, 20 sccm flux of Ar at a pressure of 20 mTorr). AZO nanostructures were fabricated by means of Focused Ion Beam with a FEI Strata DB235M system, using 30 keV ion energy and 25 pA beam current. The full pattern was obtained by sequential patterning and stitching of square tiles containing the NSs: 1x1 μm^2 tiles for the nanorods and 0.8x0.8 μm^2 tiles for the nano-Ls. SEM imaging was performed in the same FIB dual beam system.

Topographical analysis of the AZO thin films was carried out using a NTEGRA AURA AFM system (NT-MDT), operating under ambient pressure and room temperature conditions. The measurements were performed in air, in semi-contact (tapping) mode, employing commercially available silicon cantilevers with a rectangular geometry (MikroMasch HQ: CSC37/NoAl), characterized by nominal spring constants ranging from 0.2 to 0.8 N/m and resonance

frequencies between 20 and 40 kHz. Surface parameters, including the average roughness and root mean square roughness, were evaluated using the open-source software Gwyddion.

Pump-probe spectroscopy.

Spectroscopy experiments were performed on two different setups depending on the wavelength range of the probe. The experimental setup used for the infrared probe experiments exploited a regeneratively amplified Yb laser providing 50 μJ, 220-fs-long pulses at 1030 nm and 100 kHz repetition rate. The laser source was used to supply a two-stage optical parametric amplifier (OPA) capable of providing pump pulses tunable in the spectral regions between 1.1-1.8 μm and 2.5-10 μm.[38] OPA was tuned to provide 50-fs-long pulses centered at around 1600 nm and 3000 nm to excite the plasmonic resonances of the AZO thin film and the nanostructures with 15μW pulses energy. The pump beam was modulated at 50 kHz through a Pockels cell driven by a digital delay generator and acting on the OPA seed generation process. The probe beam maintained instead the same repetition rate of the laser source, with the pulses being achieved by white light generation (WLG) in a 10-mm-long YAG crystal and covering the spectral region between 1.25-2 μm. For the detection a common path interferometric spectrometer was used, followed by an InAsSb photodiode.[39] A lock-in amplifier triggered by the digital delay generator was then used to demodulate the signals from the detector and obtain both the static and differential transmission. This arrangement allowed us to achieve very high sensitivity by exploiting the advantages provided both by the laser's high repetition rate and shot-to-shot stability and by lock-in detection.

For the UV-VIS experiments we used a different laser source that gave us the capability to study close to the interband transitions of AZO. It starts from a Ti:Sapphire laser providing 4mJ, 100fs long pulses at 800nm and 1KHz repetition rate. As before, we used an OPA to generate a 1.6um pump beam with a temporal duration of around 70 fs to excite the plasmon resonance. To generate a white light spanning the range from 340 to 600 nm, we used a 2 mm thick CaF_2 crystal that was kept in rotation to avoid degradation. In this case we used a Si based optical multichannel analyzer. In both cases the pump probe delay was changed by a computer controlled mechanical delay line and recorded a differential transmittivity spectrum for every step.

Supporting Information

Supporting Information is available from the Wiley Online Library or from the author.

Data Availability Statement

The data are available from the authors upon request.

Acknowledgements

T.V. and L.B. contributed equally to the work.

The authors would like to thank Andrea Schirato for useful discussions. L.B. acknowledges financial support from Ministero dell'Università e della Ricerca (MUR) project "Progetto di Ricerca ECOSYSTEM FOR SUSTAINABLE TRANSITION IN EMILIA-ROMAGNA finanziato nell'ambito del Piano Nazionale di Ripresa e Resilienza (PNRR) – MISSIONE 4 "Istruzione Ricerca" COMPONENTE 2, "Dalla ricerca all'impresa" INVESTIMENTO 1.5, "Creazione e rafforzamento di "Ecosistemi dell'innovazione", costruzione di "leader territoriali di R&S"- finanziato dall'Unione europea – NextGenerationEU - Decreto di concessione n.0001052 del 23/06/2022 - Progetto ECS_00000033 – CUP E93C22001100001". A.C. acknowledges the National Centre for HPC, Big Data and Quantum Computing (ICSC), funded under the National Recovery and Resilience Plan (NRRP), Mission 04 Component 2 Investment 1.4, NextGenerationEU, Award Number: CN00000013. A.C. and S.B. acknowledge the financial support financial support under the National Recovery and Resilience Plan (NRRP), Mission 4, Component 2, Investment 1.1, Call for tender no. 104 PRIN 2022 funded by the European Union – NextGenerationEU – Project AMONIX – CUP B53D23004060006. M.G. thanks the sPATIALS3 project by Regione Lombardia.

Received: ((will be filled in by the editorial staff))

Revised: ((will be filled in by the editorial staff))

Published online: ((will be filled in by the editorial staff))

Tersilla Virgili, Luca Bursi, Riccardo Magrin Maffei, Michele Guizzardi, Andrea Villa, Alessandro di Bona, Andrea Mescola, Gian Carlo Gazzadi, Arrigo Calzolari, Stefania Benedetti

Controlling the static and ultra-fast infrared optical response of Al:ZnO through nanostructuration

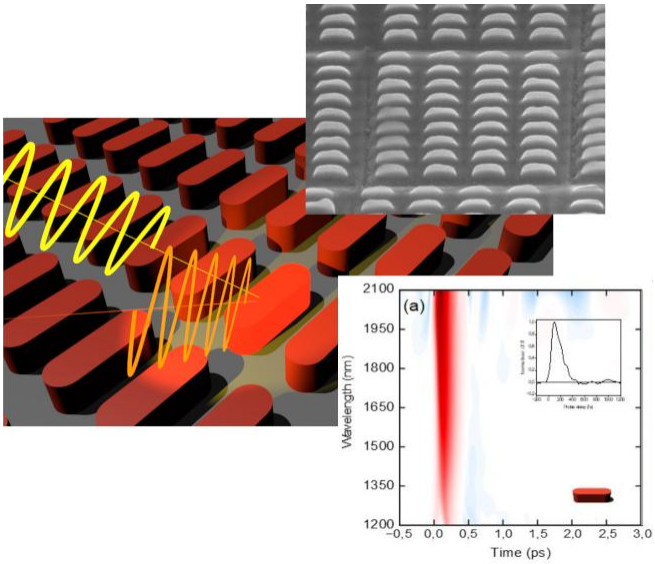

AZO nanostructuration tunes the optical properties of the material. Optimized metasurfaces are designed, fabricated, and compared after an electron beam lithography and focused ion beam process. The MID-IR pump probe characterization demonstrates that we can modify and control the ultrafast optical response of AZO by nanostructuration, making metasurfaces promising building blocks for infrared plasmonics and nanophotonic applications.

References

(1) Naik, G. V.; Shalaev, V. M.; Boltasseva, A. Alternative Plasmonic Materials: Beyond Gold and Silver. *Advanced Materials* **2013**, *25* (24), 3264-3294, Review. DOI: 10.1002/adma.201205076.
(2) Kinsey, N.; DeVault, C.; Kim, J.; Ferrera, M.; Shalaev, V. M.; Boltasseva, A. Epsilon-near-zero Al-doped ZnO for ultrafast switching at telecom wavelengths. *Optica* **2015**, *2* (7), 616-622, Article. DOI: 10.1364/optica.2.000616.
(3) Calzolari, A.; Ruini, A.; Catellani, A. Transparent Conductive Oxides as Near-IR Plasmonic Materials: The Case of Al-Doped ZnO Derivatives. *ACS PHOTONICS* **2014**, *1* (8), 703-709, Article. DOI: 10.1021/ph500118y.
(4) Lu, J. G.; Ye, Z. Z.; Zeng, Y. J.; Zhu, L. P.; Wang, L.; Yuan, J.; Zhao, B. H.; Liang, Q. L. Structural, optical, and electrical properties of (Zn,Al)O films over a wide range of compositions. *Journal of Applied Physics* **2006**, *100*, 073714. DOI: 10.1063/1.2357638.
(5) Valenti, I.; Benedetti, S.; Di Bona, A.; Lollobrigida, V.; Perucchi, A.; Di Pietro, P.; Lupi, S.; Valeri, S.; Torelli, P. Electrical, optical, and electronic properties of Al:ZnO films in a wide doping range. *Journal of Applied Physics* **2015**, *118* (16), 165304. DOI: 10.1063/1.4934512.
(6) Wang, Y.; Capretti, A.; Dal Negro, L. Wide tuning of the optical and structural properties of alternative plasmonic materials. *OPTICAL MATERIALS EXPRESS* **2015**, *5* (11), 2415-2430, Article. DOI: 10.1364/OME.5.002415.
(7) Oh, B.; Jeong, M.; Kim, D.; Lee, W.; Myoung, J. Post-annealing of Al-doped ZnO films in hydrogen atmosphere. *JOURNAL OF CRYSTAL GROWTH* **2005**, *281* (2-4), 475-480, Article. DOI: 10.1016/j.jcrysgro.2005.04.045.
(8) Feigenbaum, E.; Diest, K.; Atwater, H. A. Unity-Order Index Change in Transparent Conducting Oxides at Visible Frequencies. *Nano Letters* **2010**, *10* (6), 2111-2116, Article. DOI: 10.1021/nl1006307.
(9) Sygletou, M.; Benedetti, S.; di Bona, A.; Canepa, M.; Bisio, F.; Bellingeri, E. In-Operando Optical Spectroscopy of Field-Effect-Gated Al-Doped ZnO. *Acs Applied Materials & Interfaces* **2023**, *15*, 3112, Article; Early Access. DOI: 10.1021/acsami.2c16668.
(10) Maffei, R.; Magnozzi, M.; Sygletou, M.; Colace, S.; D'Addato, S.; Petrov, A.; Canepa, M.; Torelli, P.; di Bona, A.; Benedetti, S.; et al. Active optical modulation in hybrid transparent-conductive oxide/electro-optic multilayers. *JOURNAL OF MATERIALS CHEMISTRY C* **2025**, *13* (12), 6346-6353, Article. DOI: 10.1039/d4tc04748f.
(11) Abb, M.; Albella, P.; Aizpurua, J.; Muskens, O. All-Optical Control of a Single Plasmonic Nanoantenna-ITO Hybrid. *NANO LETTERS* **2011**, *11* (6), 2457-2463, Article. DOI: 10.1021/nl200901w.
(12) Zheludev, N.; Kivshar, Y. From metamaterials to metadevices. *NATURE MATERIALS* **2012**, *11* (11), 917-924, Review. DOI: 10.1038/NMAT3431.
(13) Yu, N.; Genevet, P.; Kats, M.; Aieta, F.; Tetienne, J.; Capasso, F.; Gaburro, Z. Light Propagation with Phase Discontinuities: Generalized Laws of Reflection and Refraction. *SCIENCE* **2011**, *334* (6054), 333-337, Article. DOI: 10.1126/science.1210713.
(14) Lin, J.; Zhong, K.; Lee, P. Plasmonic behaviors of metallic AZO thin film and AZO nanodisk array. *OPTICS EXPRESS* **2016**, *24* (5), 5125-5135, Article. DOI: 10.1364/OE.24.005125.
(15) Kim, J.; Naik, G.; Emani, N.; Guler, U.; Boltasseva, A. Plasmonic Resonances in Nanostructured Transparent Conducting Oxide Films. *IEEE JOURNAL OF SELECTED TOPICS IN QUANTUM ELECTRONICS* **2013**, *19* (3), 4601907, Article. DOI: 10.1109/JSTQE.2013.2238611.

(16) Li, S.; Guo, P.; Zhang, L.; Zhou, W.; Odom, T.; Seideman, T.; Ketterson, J.; Chang, R. Infrared Plasmonics with Indium-Tin-Oxide Nanorod Arrays. *ACS NANO* **2011**, *5* (11), 9161-9170, Article. DOI: 10.1021/nn203406f.
(17) Santiago, K.; Mundle, R.; Samantaray, C.; Bahoura, M.; Pradhan, A. Nanopatterning of atomic layer deposited Al:ZnO films using electron beam lithography for waveguide applications in the NIR region. *OPTICAL MATERIALS EXPRESS* **2012**, *2* (12), 1743-1750, Article.
(18) Gregory, S.; Wang, Y.; de Groot, C.; Muskens, O. Extreme Subwavelength Metal Oxide Direct and Complementary Metamaterials. *ACS PHOTONICS* **2015**, *2* (5), 606-614, Article. DOI: 10.1021/acsphotonics.5b00089.
(19) Kildishev, A.; Boltasseva, A.; Shalaev, V. Planar Photonics with Metasurfaces. *SCIENCE* **2013**, *339*, 1232009, Review. DOI: 10.1126/science.1232009.
(20) Yang, J.; Gurung, S.; Bej, S.; Ni, P.; Lee, H. Active optical metasurfaces: comprehensive review on physics, mechanisms, and prospective applications. *REPORTS ON PROGRESS IN PHYSICS* **2022**, *85* (3), 036101, Review. DOI: 10.1088/1361-6633/ac2aaf.
(21) Brongersma, M.; Halas, N.; Nordlander, P. Plasmon-induced hot carrier science and technology. *NATURE NANOTECHNOLOGY* **2015**, *10* (1), 25-34, Review. DOI: 10.1038/NNANO.2014.311.
(22) Vanzan, M.; Marsili, M. Theoretical approaches for the description of plasmon generated hot carriers phenomena. *NPJ COMPUTATIONAL MATERIALS* **2024**, *10* (1), 222, Review. DOI: 10.1038/s41524-024-01412-5.
(23) MacDonald, K.; Sámson, Z.; Stockman, M.; Zheludev, N. Ultrafast active plasmonics. *NATURE PHOTONICS* **2009**, *3* (1), 55-58, Article. DOI: 10.1038/nphoton.2008.249.
(24) Maiuri, M.; Garavelli, M.; Cerullo, G. Ultrafast Spectroscopy: State of the Art and Open Challenges. *JOURNAL OF THE AMERICAN CHEMICAL SOCIETY* **2020**, *142* (1), 3-15, Review. DOI: 10.1021/jacs.9b10533.
(25) Schirato, A.; Maiuri, M.; Cerullo, G.; Della Valle, G. Ultrafast hot electron dynamics in plasmonic nanostructures: experiments, modelling, design. *NANOPHOTONICS* **2023**, *12* (1), 1-28, Review. DOI: 10.1515/nanoph-2022-0592.
(26) Luo, Y.; Sun, Z.; Sun, Z.; Dai, Q. Ultrafast Infrared Plasmonics. *ADVANCED MATERIALS* **2025**, *37* (10), 2413748, Review. DOI: 10.1002/adma.202413748.
(27) Clerici, M.; Kinsey, N.; DeVault, C.; Kim, J.; Carnemolla, E.; Caspani, L.; Shaltout, A.; Faccio, D.; Shalaev, V.; Boltasseva, A.; et al. Controlling hybrid nonlinearities in transparent conducting oxides via two-colour excitation. *NATURE COMMUNICATIONS* **2017**, *8*, 15829, Article. DOI: 10.1038/ncomms15829.
(28) Ferrera, M.; Carnemolla, E. Ultra-fast transient plasmonics using transparent conductive oxides. *JOURNAL OF OPTICS* **2018**, *20* (2), 024007, Article. DOI: 10.1088/2040-8986/aa9d01.
(29) Sygletou, M.; Benedetti, S.; di Bona, A.; Canepa, M.; Bisio, F. Doping-Dependent Optical Response of a Hybrid Transparent Conductive Oxide/Plasmonic Medium. *Journal of Physical Chemistry C* **2022**, *126* (4), 1881-1889. DOI: 10.1021/acs.jpcc.1c07567.
(30) Barnes, W.; Dereux, A.; Ebbesen, T. Surface plasmon subwavelength optics. *NATURE* **2003**, *424* (6950), 824-830, Review. DOI: 10.1038/nature01937.
(31) Raether; H. *Surface
plasmons on smooth and rough surfaces and on gratings*; 1988.
(32) Zayats, A.; Smolyaninov, I.; Maradudin, A. Nano-optics of surface plasmon polaritons. *PHYSICS REPORTS-REVIEW SECTION OF PHYSICS LETTERS* **2005**, *408* (3-4), 131-314, Review. DOI: 10.1016/j.physrep.2004.11.001.
(33) Jasperson; N., S.; Schnatterly, S. E. Photon-Surface-Plasmon Coupling in Thick Ag Foils. *Phys. Rev. B* **1969**, *188*, 759.

(34) Kaspar, W.; Kreibig, U. Surface structure influences on the absorptance of thick silver films. *Surf. Sci.* **1977**, *69*, 619-636.
(35) Blemker, M.; Gibbs, S.; Raulerson, E.; Milliron, D.; Roberts, S. Modulation of the Visible Absorption and Reflection Profiles of ITO Nanocrystal Thin Films by Plasmon Excitation. *ACS PHOTONICS* **2020**, *7* (5), 1188-1196, Article. DOI: 10.1021/acsphotonics.9b01825.
(36) Besteiro, L.; Kong, X.; Wang, Z.; Hartland, G.; Govorov, A. Understanding Hot-Electron Generation and Plasmon Relaxation in Metal Nanocrystals: Quantum and Classical Mechanisms. *ACS PHOTONICS* **2017**, *4* (11), 2759-2781, Article. DOI: 10.1021/acsphotonics.7b00751.
(37) Bohren, C.; Huffman, D. R. *Absorption and Scattering of Light by Small Particles*; Wiley Science Paperback Series, 1998.
(38) Villa, A.; Ross, A.; Gotti, R.; Lamperti, M.; Scotognella, F.; Cerullo, G.; Marangoni, M. Broadly tunable mid-infrared femtosecond pulses directly generated by an optical parametric amplifier. *OSA CONTINUUM* **2021**, *4* (11), 2837-2844, Article. DOI: 10.1364/OSAC.439298.
(39) Brida, D.; Manzoni, C.; Cerullo, G. Phase-locked pulses for two-dimensional spectroscopy by a birefringent delay line. *OPTICS LETTERS* **2012**, *37* (15), 3027-3029, Article. DOI: 10.1364/OL.37.003027.